

Waveguide quantum electrodynamics with superconducting artificial giant atoms

<https://doi.org/10.1038/s41586-020-2529-9>

Received: 27 December 2019

Accepted: 1 May 2020

Published online: 29 July 2020

 Check for updates

Bharath Kannan^{1,2}✉, Max J. Ruckriegel¹, Daniel L. Campbell¹, Anton Frisk Kockum³, Jochen Braumüller¹, David K. Kim⁴, Morten Kjaergaard¹, Philip Krantz^{1,8}, Alexander Melville⁴, Bethany M. Niedzielski⁴, Antti Vepsäläinen¹, Roni Winik¹, Jonilyn L. Yoder⁴, Franco Nori^{5,6}, Terry P. Orlando^{1,2}, Simon Gustavsson¹ & William D. Oliver^{1,2,4,7}✉

Models of light–matter interactions in quantum electrodynamics typically invoke the dipole approximation^{1,2}, in which atoms are treated as point-like objects when compared to the wavelength of the electromagnetic modes with which they interact. However, when the ratio between the size of the atom and the mode wavelength is increased, the dipole approximation no longer holds and the atom is referred to as a ‘giant atom’^{2,3}. So far, experimental studies with solid-state devices in the giant-atom regime have been limited to superconducting qubits that couple to short-wavelength surface acoustic waves^{4–10}, probing the properties of the atom at only a single frequency. Here we use an alternative architecture that realizes a giant atom by coupling small atoms to a waveguide at multiple, but well separated, discrete locations. This system enables tunable atom–waveguide couplings with large on–off ratios³ and a coupling spectrum that can be engineered by the design of the device. We also demonstrate decoherence-free interactions between multiple giant atoms that are mediated by the quasi-continuous spectrum of modes in the waveguide—an effect that is not achievable using small atoms¹¹. These features allow qubits in this architecture to switch between protected and emissive configurations in situ while retaining qubit–qubit interactions, opening up possibilities for high-fidelity quantum simulations and non-classical itinerant photon generation^{12,13}.

Devices in which atoms are directly coupled to waveguides are well described by waveguide quantum electrodynamics (QED). Superconducting circuits offer an ideal platform upon which to implement and explore the physics of waveguide QED, owing to the achievable strong coupling between the atomic and photonic degrees of freedom. In superconducting waveguide QED, artificial atoms are coupled to the continuum of propagating electromagnetic modes of a one-dimensional microwave transmission line^{14,15}. The size of these atoms is typically much smaller than the wavelength of the modes in the transmission line, as depicted in Fig. 1a. Superconducting artificial atoms can be engineered to spontaneously emit most of their excitations as propagating photons in the waveguide, as opposed to other emission channels in the system. This enables a diverse and rich set of phenomena to be experimentally observed, such as resonance fluorescence^{16–19}, collective Lamb shifts²⁰ and Dicke super- and sub-radiance^{21–23}. Additionally, the one-dimensional nature of the modes enables the waveguide to mediate long-range interactions between multiple atoms^{22,24}. Very recently, in a work complementary to ours, electromagnetically induced transparency was reported using a giant superconducting artificial atom²⁵.

A central limitation of waveguide QED is the ever-present and strong dissipation of qubits into the waveguide. As a result, it is difficult to prepare many-body states of the qubits. In the context of waveguide QED, the ability to initialize and entangle qubits with high fidelity can aid in various applications. For instance, using the tunable qubit–waveguide coupling offered by giant atoms, one can perform digital–analog quantum simulations of fermion–fermion scattering via a bosonic bath^{12,26}. Additionally, the generation of non-classical itinerant microwave photons from qubit emitters that are directly coupled to a waveguide^{13,27} can be applied in quantum communication and teleportation protocols^{28,29}. Recently, correlated dissipation between qubits was used to prepare entangled dark states that are decoupled from the waveguide²³. However, only a fraction of the total qubit Hilbert space is protected from dissipation with this approach.

In this work, we overcome this obstacle using an appropriate arrangement of giant atoms along a waveguide that protects the entire Hilbert space of the qubits while preserving waveguide-mediated qubit–qubit interactions¹¹. We show how the geometry of the giant atoms can be altered to engineer the qubit–waveguide and qubit–qubit couplings. We then use this engineered spectrum to prepare entangled states of

¹Research Laboratory of Electronics, Massachusetts Institute of Technology, Cambridge, MA, USA. ²Department of Electrical Engineering and Computer Science, Massachusetts Institute of Technology, Cambridge, MA, USA. ³Wallenberg Centre for Quantum Technology, Department of Microtechnology and Nanoscience, Chalmers University of Technology, Gothenburg, Sweden. ⁴MIT Lincoln Laboratory, Lexington, MA, USA. ⁵Theoretical Quantum Physics Laboratory, RIKEN Cluster for Pioneering Research, Wako, Japan. ⁶Department of Physics, The University of Michigan, Ann Arbor, MI, USA. ⁷Department of Physics, Massachusetts Institute of Technology, Cambridge, MA, USA. ⁸Present address: Wallenberg Centre for Quantum Technology, Department of Microtechnology and Nanoscience, Chalmers University of Technology, Gothenburg, Sweden. ✉e-mail: bkannan@mit.edu; william.oliver@mit.edu

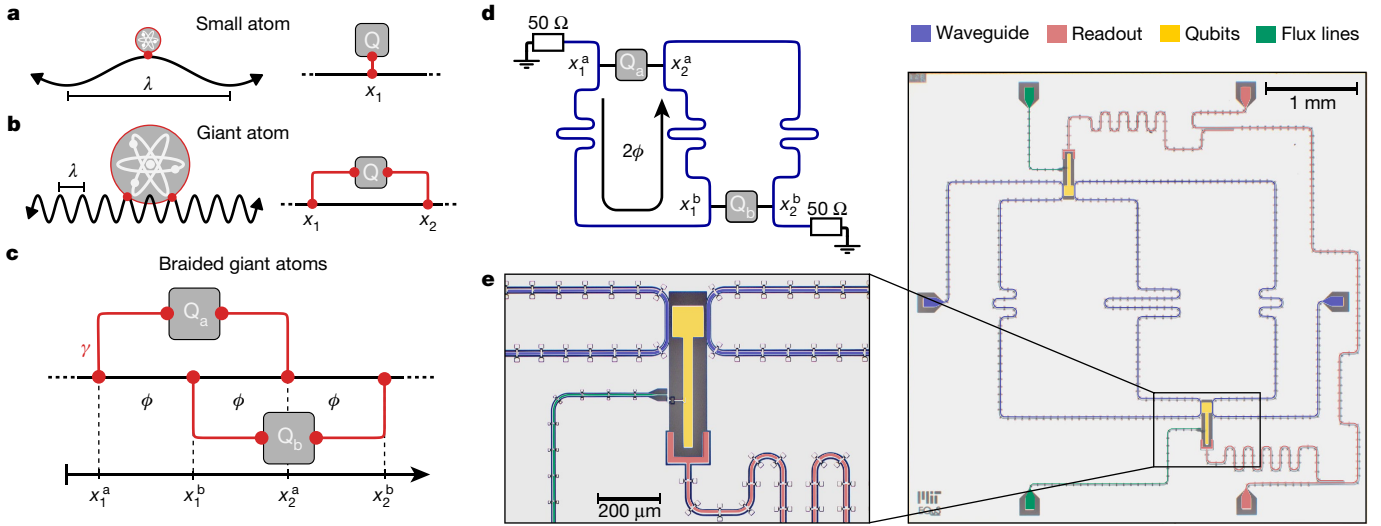


Fig. 1 | Giant atoms with superconducting qubits. **a**, A schematic diagram of a small atom. The small atom is treated as a point-like object because it is much smaller than λ , the wavelength of the mode it interacts with. **b**, A giant atom, formed by coupling a small atom to a mode at two discrete, distant locations. **c**, The configuration of two braided giant atoms, coupled twice to a waveguide with equal strength. The phase difference between coupling points

$\phi = \omega(x_1^b - x_1^a)/v = \omega(x_2^a - x_1^b)/v = \omega(x_2^b - x_2^a)/v$ is varied by tuning the qubit frequencies ω . **d, e**, A schematic diagram (**d**) and a false-colour optical micrograph image (**e**) of a device in the configuration shown in **c**. Each qubit (yellow) has a readout resonator (red) and flux line (green) for independent readout and flux control. The central waveguide (blue) is terminated to 50 Ω .

the qubits and show that, even in the presence of a waveguide, giant atoms can be used to perform coherent quantum operations.

Our devices consist of two frequency-tunable transmon qubits³⁰, Q_a and Q_b , each of which is coupled to a superconducting resonator for dispersive readout³¹. The signal from the resonators is first amplified by a travelling-wave parametric amplifier³² to maximize the readout efficiency. We construct giant atoms of the form shown in Fig. 1b by coupling the qubits to a 50- Ω coplanar waveguide at two locations. The qubits are coupled to the waveguide in a braided manner, as shown in Fig. 1c, d, such that the first coupling point of qubit Q_b at x_1^b is centred between the coupling points of qubit Q_a at x_1^a and x_2^a . Photons in the waveguide will experience a phase shift $\phi = 2\pi\Delta x/\lambda(\omega)$ between neighbouring coupling points, depending on the spatial separation between successive coupling points Δx and the wavelength $\lambda(\omega)$ for modes at the qubit frequencies $\omega = \omega_{a,b}$. The phase ϕ can then be tuned in situ by changing the qubit frequencies, and thereby the wavelength $\lambda(\omega) = 2\pi v/\omega$, where v is the speed of light in the waveguide. The device is designed symmetrically such that $\Delta x = x_1^b - x_1^a = x_2^a - x_1^b = x_2^b - x_2^a$. Moreover, the individual physical couplings between the qubits and the waveguide are designed to be of equal strength, $\gamma(\omega) = \gamma_0(\omega/\omega_0)^2$, where γ_0 is the coupling strength at a reference frequency ω_0 . Under these conditions, the interaction Hamiltonian between the qubits and the waveguide is

$$\hat{H}_I = \hbar \sum_{k,j} J(\omega_k) \hat{\sigma}_x^{(j)} [\hat{a}_{k,L}^\dagger A_j(\omega_k) + \hat{a}_{k,R}^\dagger A_j^*(\omega_k) + \text{h.c.}], \quad (1)$$

where the sum over k indexes the quasi-continuum of modes in the waveguide, $j \in \{a, b\}$ is summed over the qubits and h.c. is the Hermitian conjugate. The coupling strength $J(\omega_k)$ between the qubits and the k th mode of the waveguide determines the physical qubit-waveguide coupling at the qubit frequency ω ,

$$\gamma(\omega) = 4\pi J(\omega)^2 D(\omega), \quad (2)$$

where $D(\omega)$ is the density of states in the waveguide³. We further distinguish between left- and right-propagating waveguide modes with the subscripts L, R in the creation operators $\hat{a}_{k,L}^\dagger$ and $\hat{a}_{k,R}^\dagger$. The qubit Pauli X operators $\hat{\sigma}_x^{(j)}$ mediate the excitation exchange to and from the qubits. The effect of coupling the qubits at multiple points along the

waveguide is accounted for by modifying the complex coupling amplitude

$$A_j(\omega) = \sum_n e^{-i\omega x_n^{(j)}/v}. \quad (3)$$

This is the sum over all phase factors for each connection point $n \in \{1, 2\}$ of qubit Q_j at positions $x_n^{(j)}$ along the waveguide. This frequency-dependent amplitude captures all interference effects between the coupling points of both giant atoms.

To characterize this system, we first detune the qubits away from each other, such that $|\omega_a - \omega_b| \gg \gamma$, and probe the properties of the giant atoms independently. The relaxation rates $\Gamma_1 = T_1^{-1}$ for the qubits are obtained by measuring the qubit energy relaxation time T_1 as a function of the qubit frequency. We show three representative T_1 traces in Fig. 2a for different qubit frequencies. The relaxation rates over a wide range of qubit frequencies are shown in Fig. 2b. For each qubit, the expression for Γ_1 is¹¹

$$\Gamma_1 = 2\gamma(\omega)[1 + \cos(2\phi)] + \gamma_{nr}, \quad (4)$$

where γ_{nr} is the intrinsic ‘non-radiative’ qubit lifetime limited by decay channels other than loss into the waveguide³³. The qubit relaxation rate depends strongly on the phase ϕ and, thereby, the qubit frequency. This is due to quantum interference between photons emitted into the waveguide at the two coupling points of the qubit. At $2\phi = \pi$, the qubit will, in effect, decouple from relaxation into the waveguide, owing to destructive interference. We observe this phenomenon when the qubit is set to the decoherence-free frequency $\omega_{DF}/2\pi = 4.645$ GHz. Here, the lifetime of the qubit is measured to be $T_1 = 31.5 \mu\text{s}$, consistent with the typical lifetime of tunable transmon qubits in a cavity QED architecture³⁴, despite its strong physical couplings to the continuum of modes in a waveguide. This indicates that the qubit relaxation into the waveguide is largely suppressed. The fitted theory curve of equation (4) in Fig. 2b is in good agreement with the measured data, from which $\gamma_0/2\pi = 2$ MHz and $\gamma_{nr}/2\pi \approx 0.03$ MHz at $\omega_0 = \omega_{DF}$ are inferred. We perform the same measurement and fit on Q_b to verify that its γ_0 and ω_{DF} are identical to those of Q_a .

Next, we investigate waveguide-mediated qubit-qubit interactions. We extract the interaction strength from a fit to the avoided level

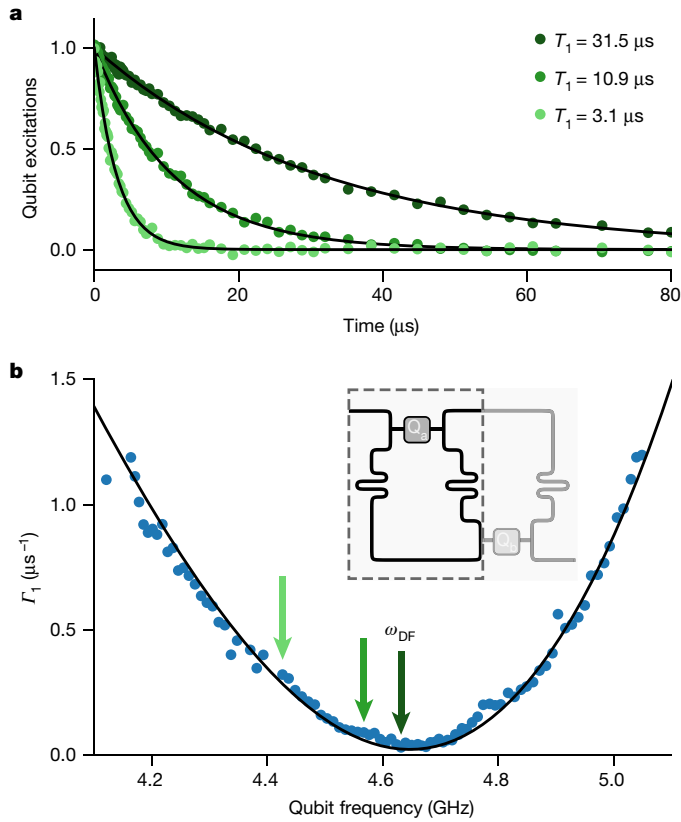


Fig. 2 | Tunable coupling for a single giant atom. a, T_1 traces and fits for qubit Q_a at three different qubit frequencies. The fitted T_1 values are given in the top right. **b**, The measured relaxation rate $\Gamma_1 = T_1^{-1}$ for qubit Q_a as a function of its frequency, with the fit to the theory (solid line). The three green arrows correspond to the relaxation rate for the T_1 traces shown in **a**. The qubit decouples from the waveguide at a decoherence-free frequency $\omega_{DF}/2\pi = 4.645$ GHz with a lifetime of $T_1 = 31.5$ μ s.

crossings observed in qubit spectroscopy, performed for various qubit frequencies. The measured and fitted interaction strengths are shown in Fig. 3a. Of particular note is the finite exchange interaction at the decoherence-free frequency $\omega_{DF} = \omega_a = \omega_b$, for which the avoided level crossing is shown in Fig. 3b. The waveguide continues to mediate interactions between the qubits even though the qubits are decoupled from relaxation into it. This can be understood by considering the device geometry. With small atoms, atomic exchange interactions are mediated by virtual photons in the waveguide that are emitted and absorbed by different atoms. The strength of these interactions, $g = \gamma \sin(\theta)/2$, is periodic in the phase delay θ between the coupling points of the small atoms²⁴. A similar effect occurs with multiple giant atoms coupled to a waveguide. In our device, the total exchange interaction is obtained by summing the contribution from all four possible pairs of coupling points between the two qubits. For our braided configuration, the virtual photons emitted and absorbed by the three consecutive coupling pairs ($x_1^a \leftrightarrow x_1^b$), ($x_1^a \leftrightarrow x_2^b$) and ($x_2^a \leftrightarrow x_2^b$) will contribute $\gamma \sin(\phi)/2$ to the interaction strength. The pair formed by the two outermost points, ($x_1^a \leftrightarrow x_2^b$), will contribute $\gamma \sin(3\phi)/2$. The interaction strength between the braided giant atoms in our device is then given by

$$g = \frac{\gamma(\omega)}{2} [3\sin(\phi) + \sin(3\phi)]. \quad (5)$$

At the decoherence-free frequency, we have $\phi = \pi/2$ and, therefore, a net interaction strength $g = \gamma$. This effect, where $\Gamma_1 = 0$ and $g \neq 0$, is unique to braided configurations of giant atoms¹¹ and is a necessary condition for high-fidelity state preparation of qubits coupled to a waveguide.

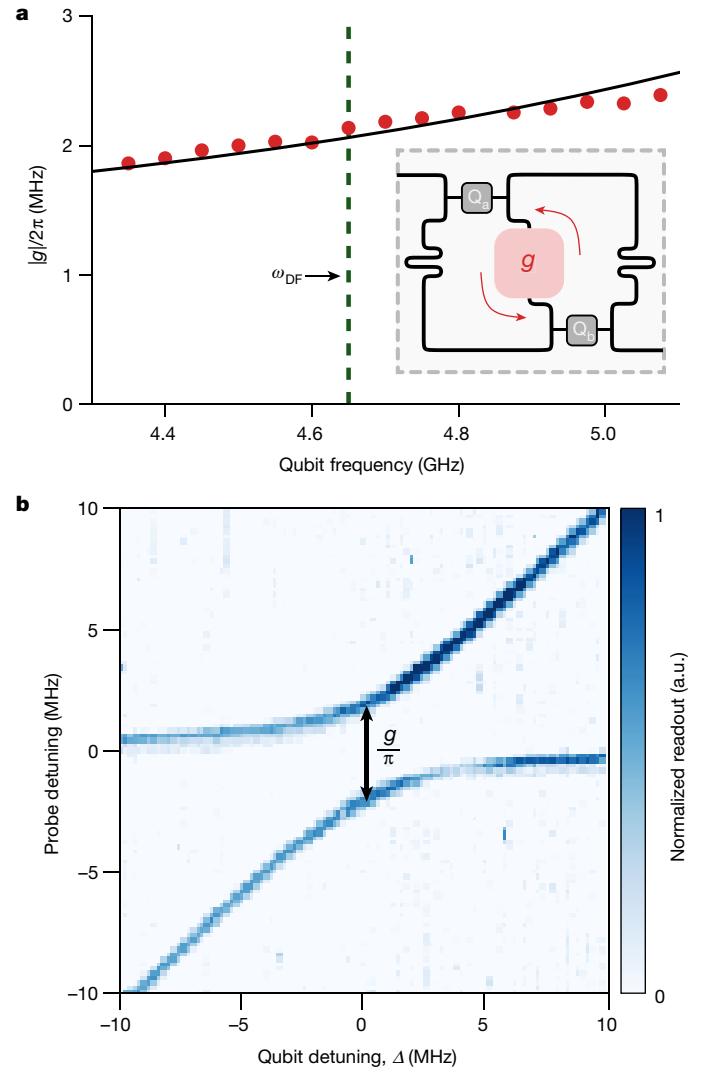


Fig. 3 | Decoherence-free interactions between two giant atoms. a, The measured exchange-interaction strengths between the qubits from avoided level crossings as a function of the qubit frequencies. The fit to theory (solid line) is plotted with the data (red dots) and the decoherence-free frequency is shown (dashed line). **b**, The qubit spectroscopy of an avoided level crossing centred at the decoherence-free frequency $\omega_{DF}/2\pi = 4.645$ GHz. The frequency of the applied drive is swept to probe the qubit frequencies for multiple qubit detunings Δ . The readout signals for each qubit are normalized and summed together to obtain both branches of the crossing. Even though the qubits are decoupled from spontaneous emission into the waveguide, a qubit exchange interaction that is mediated by virtual photons in the waveguide is measured to be $g/2\pi = 2$ MHz.

The spectra presented in Figs. 2b, 3a are largely determined by the geometry of the device. That is, one can vary the number of coupling points, their relative coupling strengths and the distance between them to tailor the frequency dependence of the qubit–waveguide and qubit–qubit coupling rates. As a demonstration of this, we probe a device with a geometry such that qubit relaxation and exchange can be simultaneously suppressed. We then use this property to perform entangling gates between the qubits. The device consists of two qubits that are each coupled to a waveguide at three locations, and is parameterized by three distinct phase delays (ϕ_1 , ϕ_2 and ϕ_3), as shown in Fig. 4a. The device is designed such that the physical qubit–waveguide coupling strengths are γ_1 at $x_1^{a,b}$ and $x_3^{a,b}$, and γ_2 at $x_2^{a,b}$. The relaxation times and qubit–qubit coupling strengths are (see Methods for derivation):

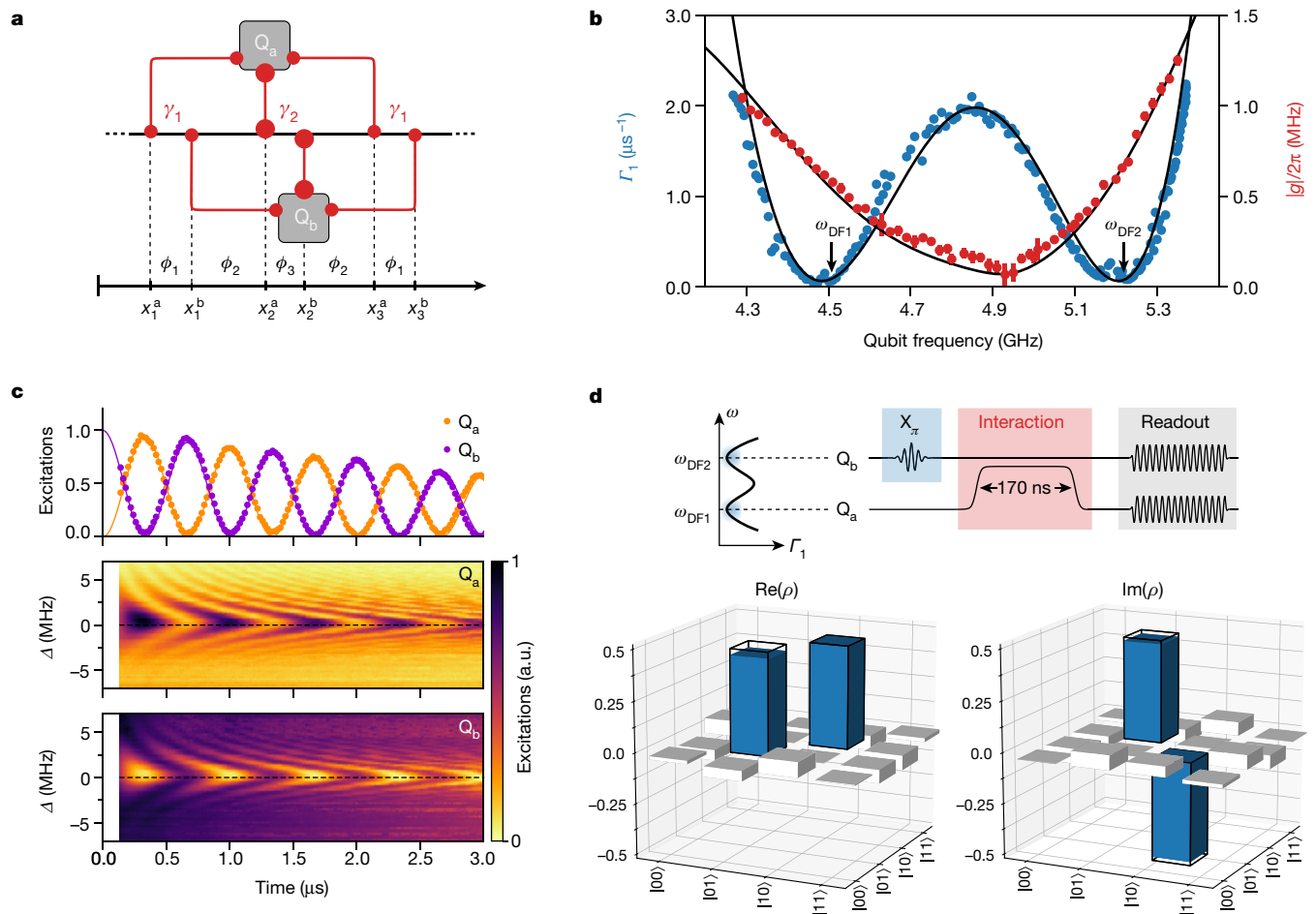


Fig. 4 | Entangling qubits in waveguide QED with engineered giant-atom geometries. **a**, A schematic diagram of a giant-atom device with two qubits coupled to the waveguide at three points. The first and last coupling points for each qubit are designed to be equal in strength (γ_1), and the central coupling point is larger ($\gamma_2 > \gamma_1$). The ratios ϕ_1/ϕ_2 , ϕ_1/ϕ_3 and ϕ_2/ϕ_3 are fixed in hardware by the relative length of the waveguide segments. **b**, The measured and fitted single-qubit relaxation rates (blue) and resonant $\Delta = 0$ exchange-interaction strengths between Q_a and Q_b (red) for the configuration of giant atoms shown in **a**. The error bars show the standard deviation of the fitted value; some errors are smaller than the symbol size. The design has two decoherence-free frequencies at $\omega_{DF1}/2\pi = 4.51$ GHz and $\omega_{DF2}/2\pi = 5.23$ GHz. The coupling strengths inferred from the fits are $\gamma_1/2\pi = 1.58$ MHz and $\gamma_2/2\pi = 3.68$ MHz at a

$$\Gamma_1 = \gamma_2 + 2\gamma_1[1 + \cos(\phi_1 + 2\phi_2 + \phi_3)] + 2\sqrt{\gamma_1\gamma_2}[\cos(\phi_1 + \phi_2) + \cos(\phi_2 + \phi_3)] + \gamma_{nr}, \quad (6)$$

$$g = \sqrt{\gamma_1\gamma_2}[\sin(\phi_2) + \sin(\phi_1 + \phi_2 + \phi_3)] + \frac{\gamma_1}{2}[2\sin(\phi_1) + \sin(2\phi_2 + \phi_3) + \sin(2\phi_1 + 2\phi_2 + \phi_3)] + \frac{\gamma_2}{2}\sin(\phi_3). \quad (7)$$

From length measurements and microwave simulations of the different sections of the waveguide, we find the ratios between the phase delays to be $\phi_1 = \phi_3 = 0.505\phi_2$. Fixing these ratios, we fit the spectra and infer the coupling strengths to be $\gamma_1/2\pi = 1.58$ MHz and $\gamma_2/2\pi = 3.68$ MHz at a reference frequency $\omega_0/2\pi = 5.23$ GHz. With this geometry, we are able to engineer the relaxation spectra for both qubits to have two decoherence-free frequencies separated by 720 MHz, $\omega_{DF1}/2\pi = 4.51$ GHz and $\omega_{DF2}/2\pi = 5.23$ GHz. Thus, each qubit can be placed at a unique decoherence-free frequency to simultaneously protect them from

reference frequency $\omega_0/2\pi = 5.23$ GHz. **c**, The time-domain chevron pattern demonstrating the exchange coupling between the qubits at the upper decoherence-free frequency ω_{DF2} as a function of interaction time and qubit-qubit detuning Δ . The excitation will swap maximally with a period $\pi/g = 680$ ns when $\Delta = 0$ and is suppressed as $|\Delta|$ increases. **d**, Top, the pulse sequence for preparing the entangled state $(|01\rangle - i|10\rangle)/\sqrt{2}$. Q_a is placed at ω_{DF1} , and Q_b is placed at ω_{DF2} and excited with a π pulse. Q_a is then brought onto resonance $\Delta = 0$ and interacts with Q_b for a time $\pi/4g = 170$ ns. Q_a is then returned to ω_{DF1} and tomography readout pulses are applied. Bottom, the real and imaginary parts of the qubit density matrix obtained for this pulse sequence, with matrix elements—ideally non-zero—shaded in blue. The state-preparation fidelity is 94%.

relaxation into the waveguide and suppress exchange interactions between them. The asymmetry in the measured spectra in Fig. 4b is due to the frequency dependence of the coupling strengths $\gamma_{1,2} \propto \omega^2$ as well as a small deviation from the desired design ($\phi_1 = 0.5\phi_2$). We observe a small deviation from theory in the spectrum for g . Ideally, the exchange interaction would be zero at $\omega/2\pi = 4.95$ GHz. However, from our fit, we extract a small non-zero parasitic interaction that is given by the minimum value of $|g(\omega)/2\pi| \approx 70$ kHz. Taking this parasitic coupling into account, we find very good agreement between the overall spectra and theory.

We use this engineered spectrum with two decoherence-free frequencies to demonstrate that giant atoms can be used to prepare entangled states in waveguide QED devices. When placed on resonance at ω_{DF2} , the qubits exchange excitations at a rate $g/2\pi = 735$ kHz. We confirm this by observing the chevron pattern formed by this excitation swap as a function of the interaction time and qubit-qubit detuning Δ in Fig. 4c. Using the pulse sequence shown in Fig. 4d, we perform an entangling \sqrt{i} SWAP operation to prepare the state $(|01\rangle - i|10\rangle)/\sqrt{2}$.

The density matrix ρ is obtained from a maximum-likelihood estimation on the two-qubit state tomography and is shown in Fig. 4d. After correcting for readout errors³⁵, we find a state-preparation fidelity of $\text{tr}(\sqrt{\sigma}\rho\sqrt{\sigma})^2 = 94\%$, where σ is the ideal density matrix. This demonstrated ability to entangle qubits using purely coherent interactions is a hallmark feature of giant atoms that are coupled to a waveguide. Furthermore, the entire two-qubit Hilbert space is protected from dissipation into the waveguide, and so a combination of iSWAP and single-qubit gates can be used to prepare any state.

Looking forward, giant atoms offer a practical way to couple distant qubits. Conventionally, this is accomplished by coupling qubits via a resonator. However, the lower free spectral range of longer resonators imposes a limit on the maximum detuning between qubits and increases their Purcell decay. Giant atoms in waveguide QED are not subject to either of these constraints, because the waveguide consists of a continuum of modes and the suppression of relaxation is due to interference. Therefore, these devices can be scaled to a greater number of qubits that are farther separated. For example, the architecture studied in this work can be naturally extended to perform quantum simulations of spin models with nearest-neighbour or all-to-all long-distance interactions¹¹. These non-local interactions may also prove useful in quantum error-correction schemes that go beyond the nearest-neighbour coupling that is native to superconducting qubits³⁶.

Finally, in standard resonator- or waveguide-based architectures, the protection of qubits for high-fidelity control and the rapid emission of quantum information as itinerant photons are generally in competition with each other. We have shown that it is possible to perform high-fidelity quantum gates with qubits that are in the presence of a waveguide and to switch between highly protected and emissive configurations. This enables giant atoms to be used as a high-quality source of itinerant quantum information; qubits can be initialized and entangled while biased at decoherence-free frequencies, and subsequently can release the quantum information they store into photons by tuning them to a frequency with strong qubit–waveguide coupling. Given an appropriate arrangement of qubits along the waveguide, this property can be used to generate itinerant photons with spatial entanglement³⁷ or entangled cluster states for measurement-based quantum computing³⁸. These sources of non-classical photons can be used in applications such as distributing entanglement and shuttling information in extensible quantum processors and networks.

Online content

Any methods, additional references, Nature Research reporting summaries, source data, extended data, supplementary information, acknowledgements, peer review information; details of author contributions and competing interests; and statements of data and code availability are available at <https://doi.org/10.1038/s41586-020-2529-9>.

1. Walls, D. F. & Milburn, G. J. *Quantum Optics* 2nd edn (Springer, 2008).
2. Kockum, A. F. Quantum optics with giant atoms – the first five years. In *International Symposium on Mathematics, Quantum Theory, and Cryptography. Mathematics for Industry* Vol. 33 (eds Takagi, T. et al.) <https://doi.org/10.1007/978-981-15-5191-8> (Springer, 2020).
3. Kockum, A. F., Delsing, P. & Johansson, G. Designing frequency-dependent relaxation rates and Lamb shifts for a giant artificial atom. *Phys. Rev. A* **90**, 013837 (2014).
4. Manenti, R. et al. Circuit quantum acoustodynamics with surface acoustic waves. *Nat. Commun.* **8**, 975 (2017).

5. Bolgar, A. N. et al. Quantum regime of a two-dimensional phonon cavity. *Phys. Rev. Lett.* **120**, 223603 (2018).
6. Moores, B. A., Sletten, L. R., Viennot, J. J. & Lehnert, K. W. Cavity quantum acoustic device in the multimode strong coupling regime. *Phys. Rev. Lett.* **120**, 227701 (2018).
7. Sletten, L. R., Moores, B. A., Viennot, J. J. & Lehnert, K. W. Resolving phonon Fock states in a multimode cavity with a double-slit qubit. *Phys. Rev. X* **9**, 021056 (2019).
8. Gustafsson, M. V. et al. Propagating phonons coupled to an artificial atom. *Science* **346**, 207–211 (2014).
9. Andersson, G., Ekström, M. K. & Delsing, P. Electromagnetically induced acoustic transparency with a superconducting circuit. *Phys. Rev. Lett.* **124**, 240402 (2020).
10. Roy, D., Suri, B., Guo, L., Aref, T. & Delsing, P. Non-exponential decay of a giant artificial atom. *Nat. Phys.* **15**, 1123–1127 (2019).
11. Kockum, A. F., Johansson, G. & Nori, F. Decoherence-free interaction between giant atoms in waveguide quantum electrodynamics. *Phys. Rev. Lett.* **120**, 140404 (2018).
12. García-Álvarez, L. et al. Fermion–fermion scattering in quantum field theory with superconducting circuits. *Phys. Rev. Lett.* **114**, 070502 (2015).
13. González-Tudela, A., Paulisch, V., Chang, D. E., Kimble, H. J. & Cirac, J. I. Deterministic generation of arbitrary photonic states assisted by dissipation. *Phys. Rev. Lett.* **115**, 163603 (2015).
14. Roy, D., Wilson, C. M. & Firstenberg, O. Strongly interacting photons in one-dimensional continuum. *Rev. Mod. Phys.* **89**, 021001 (2017).
15. Gu, X., Kockum, A. F., Miranowicz, A., Liu, Y. & Nori, F. Microwave photonics with superconducting quantum circuits. *Phys. Rep.* **718–719**, 1–102 (2017).
16. Astafiev, O. et al. Resonance fluorescence of a single artificial atom. *Science* **327**, 840–843 (2010).
17. Hoi, I.-C. et al. Demonstration of a single-photon router in the microwave regime. *Phys. Rev. Lett.* **107**, 073601 (2011).
18. Hoi, I.-C. et al. Microwave quantum optics with an artificial atom in one-dimensional open space. *New J. Phys.* **15**, 025011 (2013).
19. Hoi, I.-C. et al. Probing the quantum vacuum with an artificial atom in front of a mirror. *Nat. Phys.* **11**, 1045–1049 (2015).
20. Wen, P. Y. et al. Large collective Lamb shift of two distant superconducting artificial atoms. *Phys. Rev. Lett.* **123**, 233602 (2019).
21. Dicke, R. H. Coherence in spontaneous radiation processes. *Phys. Rev.* **93**, 99–110 (1954).
22. van Loo, A. F. et al. Photon-mediated interactions between distant artificial atoms. *Science* **342**, 1494–1496 (2013).
23. Mirhosseini, M. et al. Cavity quantum electrodynamics with atom-like mirrors. *Nature* **569**, 692–697 (2019).
24. Lalumière, K. et al. Input–output theory for waveguide QED with an ensemble of inhomogeneous atoms. *Phys. Rev. A* **88**, 043806 (2013).
25. Vadiraj, A. M. et al. Engineering the level structure of a giant artificial atom in waveguide quantum electrodynamics. Preprint at <https://arxiv.org/abs/2003.14167> (2020).
26. Lamata, L., Parra-Rodríguez, A., Sanz, M., & Solano, E. Digital–analog quantum simulations with superconducting circuits. *Adv. Phys. X* **3**, 1457981 (2018).
27. Forn-Díaz, P. et al. On-demand microwave generator of shaped single photons. *Phys. Rev. Appl.* **8**, 054015 (2017).
28. Kimble, H. J. The quantum internet. *Nature* **453**, 1023–1030 (2008).
29. O’Brien, J. L., Furusawa, A. & Vuckovic, J. Photonic quantum technologies. *Nat. Photon.* **3**, 687–695 (2009).
30. Koch, J. et al. Charge-insensitive qubit design derived from the Cooper pair box. *Phys. Rev. A* **76**, 042319 (2007).
31. Blais, A., Huang, R.-S., Wallraff, A., Girvin, S. M. & Schoelkopf, R. J. Cavity quantum electrodynamics for superconducting electrical circuits: an architecture for quantum computation. *Phys. Rev. A* **69**, 062320 (2004).
32. Macklin, C. et al. A near–quantum-limited Josephson traveling-wave parametric amplifier. *Science* **350**, 307–310 (2015).
33. Lu, Y. et al. Characterizing decoherence rates of a superconducting qubit by direct microwave scattering. Preprint at <https://arxiv.org/abs/1912.02124> (2019).
34. Kjaergaard, M. et al. Superconducting qubits: current state of play. *Annu. Rev. Condens. Matter Phys.* **11**, 369–395 (2020).
35. Chow, J. M. et al. Detecting highly entangled states with a joint qubit readout. *Phys. Rev. A* **81**, 062325 (2010).
36. Campbell, E. T., Terhal, B. M. & Vuillot, C. Roads towards fault-tolerant universal quantum computation. *Nature* **549**, 172–179 (2017); correction **559**, E6 (2018).
37. Kannan, B. et al. Generating spatially entangled itinerant photons with waveguide quantum electrodynamics. Preprint at <https://arxiv.org/abs/2003.07300> (2020).
38. Pichler, H., Choi, S., Zoller, P. & Lukin, M. D. Universal photonic quantum computation via time-delayed feedback. *Proc. Natl Acad. Sci. USA* **114**, 11362–11367 (2017).

Publisher’s note Springer Nature remains neutral with regard to jurisdictional claims in published maps and institutional affiliations.

© The Author(s), under exclusive licence to Springer Nature Limited 2020

Experimental setup

The experiments are performed in a dilution refrigerator (Bluefors XLD600), capable of cooling to a base temperature of 10 mK. The experimental setup used for all of the data presented in the main text is shown in Extended Data Fig. 1. The readout and qubit drives are all combined at room temperature (300 K) and sent into the line to which the readout resonators are coupled. This line is attenuated by 20 dB at the 4 K stage, 10 dB at the still, and 40 dB at the mixing chamber to ensure proper thermalization of the line. The samples are magnetically shielded at the mixing chamber by superconducting and Cryoperm-10 shields. To maximize the signal-to-noise ratio of the readout, a Josephson travelling-wave parametric amplifier (TWPA) is used as the first amplifier in the measurement chain. The TWPA is pumped in the forward direction using a directional coupler. A circulator is placed between the sample and the TWPA to ensure that the TWPA sees a 50- Ω impedance on both sides. The signal is then filtered with 3-GHz high-pass and 12-GHz low-pass filters. Two additional circulators are placed after the TWPA in the mixing chamber to prevent noise from higher-temperature stages travelling back into the TWPA and the sample. High-electron-mobility transistor amplifiers are used at the 4-K and room-temperature stages of the measurement chain for further amplification. The signal is then downconverted to an intermediate frequency using an IQ mixer, filtered, digitized and demodulated.

The central waveguide of the device to which the qubits couple is directly terminated to 50 Ω at the device package. This minimizes impedance mismatches that would otherwise come from external components, such as circulators and filters, which may alter the frequency dependence of the qubit–waveguide coupling strength. The frequencies of the qubits are controlled with local flux lines. Each flux line has both d.c. and radiofrequency control that are combined and filtered with 300-MHz low-pass filters at the mixing chamber. The radiofrequency flux control line is attenuated by 20 dB at the 4 K stage and by 10 dB at the still. A 1-k Ω resistor is placed in series with the d.c. voltage source to generate a d.c. current.

Flux cross-talk calibration

All devices used in the experiment had local flux lines for independent flux control, and it was necessary to calibrate the cross-talk between these lines. We measure the frequencies of both qubits as a function of the voltage applied to each flux line. The frequency spectrum of qubit i from the flux line of qubit j is fit to the analytical transmon frequency spectrum $f_{i,j}(V_j)$, approximately given by³⁰

$$f_{i,j} = f_{i,\max} 4 \sqrt{d^2 + (1-d^2)\cos^2\left(\pi \frac{V_j}{V_{0,i,j}} - \phi_0\right)}, \quad (8)$$

where $d = f_{i,\min}/f_{i,\max}$ describes the asymmetry between the junctions in the transmon SQUID (superconducting quantum interference device) loop, ϕ_0 is the offset from zero, V_i is the voltage applied on the flux line, and $f_{i,\min}$ and $f_{i,\max}$ are the minimum and maximum frequencies of the transmon, respectively. The fit parameter $V_{0,i,j}$ describes the voltage required to supply a flux quantum Φ_0 . These values for all combinations of $i, j \in \{a, b\}$ can be used to construct a cross-talk matrix S , where the matrix elements of S are given by $S_{i,j} = V_{0,i,j}^{-1}$. An example of the matrix S (in units of Φ_0^{-1}) used in the experiment is given by

$$S = \begin{pmatrix} 4.46^{-1} & 98.8^{-1} \\ 103.4^{-1} & 4.26^{-1} \end{pmatrix} \quad (9)$$

Here, the diagonal matrix elements correspond to the coupling between a qubit and its own local flux line, whereas the off-diagonal elements represent the coupling between a qubit and the other qubits flux line. The qubit frequencies $f_{i,i}$ from equation (8) can also be expressed in

terms of the flux applied on qubit i using the relation $\Phi_i = \Phi_0 V_i / V_{0,i,i}$. Thus, a desired configuration of qubit frequencies $f = (f_a, f_b)$ can be mapped onto a set of fluxes $\Phi = (\Phi_a, \Phi_b)$. The voltage configuration $V = (V_a, V_b)$ required to achieve the desired flux configuration—and therefore the desired qubit frequencies—can then be found by using the inverted cross-talk matrix $V = S^{-1}\Phi$.

Summary of device parameters

To obtain the data presented in Figs. 2, 3 we used two devices, device A and device B, which were nominally identical to each other apart from their maximum and minimum qubit frequencies. This let us obtain the coupling spectra from 4.2 GHz to 5.1 GHz. Devices A and B were used for data points in the range of qubit frequencies 4.2–4.7 GHz and 4.7–5.1 GHz, respectively. The general qubit and readout parameters for these devices are summarized in Extended Data Table 1. Similarly, a summary of the qubit and readout parameters for the device used for the data presented in Fig. 4, device C, is also given in Extended Data Table 1. An optical image of device C is shown in Extended Data Fig. 2b. Here, it can be seen that the relative coupling strength between γ_1 and γ_2 is determined by the difference in capacitance between the qubit and the waveguide at the respective coupling points.

Entangling pulse sequence

As shown in Fig. 4d, we initialize the frequencies of Q_a and Q_b to ω_{DF1} and ω_{DF2} , respectively. This protects both qubits from dissipation into the waveguide and also suppresses the exchange interaction between them with a large detuning. Next, we excite Q_b with a π pulse and bring Q_a onto resonance with it for a time $\pi/4g = 170$ ns to entangle the qubits. We then bring Q_a back to ω_{DF1} to turn the interaction off and perform two-qubit state tomography.

Relaxation and coupling spectra for generalized giant atoms

The properties of a generalized giant-atom system composed of N qubits, and in which the j th atom has M_j coupling points, can be calculated using the SLH (scattering operator, Lindblad operators, Hamiltonian) formalism for cascaded quantum systems¹¹. The qubit–waveguide coupling strength for the n th coupling point of atom j is given by $\gamma_{j,n}$ and the phase delay between the n th and m th coupling points of atoms j and k is given by ϕ_{j_n, k_m} . The master equation for this setup is given by

$$\begin{aligned} \dot{\rho} = & -i \left[\sum_{j=1}^N \omega_j' \frac{\sigma_z^{(j)}}{2} + \sum_{j=1}^{N-1} \sum_{k=j+1}^N g_{j,k} (\sigma_-^{(j)} \sigma_+^{(k)} + \sigma_+^{(j)} \sigma_-^{(k)}) \right] \rho \\ & + \sum_{j=1}^N \Gamma_j \mathcal{D}[\sigma_-^{(j)}] \rho \\ & + \sum_{j=1}^{N-1} \sum_{k=j+1}^N \Gamma_{\text{coll},j,k} \left[(\sigma_-^{(j)} \rho \sigma_+^{(k)} - \frac{1}{2} \{ \sigma_+^{(j)} \sigma_-^{(k)}, \rho \}) + \text{h.c.} \right], \end{aligned} \quad (10)$$

where $\mathcal{D}[O]\rho = O\rho O^\dagger - 1/2\{O^\dagger O, \rho\}$ is the standard Lindblad dissipator and ω_j' is the frequency of the j th atom with the Lamb shifts included. This master equation assumes weak coupling, $\gamma_{j_n} \ll \omega_j'$, and a negligible travel time between coupling points such that $\gamma_{j_n}^{-1} \gg t$, where t is the travel time for photons in the waveguide between the coupling points. Note that the latter assumption places a limit on the spatial separation Δx between coupling points, but this limit is easily satisfied in superconducting coplanar waveguides for typical values of γ_{j_n} . For example, with typical values of γ_{j_n} , the distance between the qubits would need to be of the order of $\Delta x \approx 10$ m to reach $\gamma_{j_n}^{-1} = t$.

The relaxation rate Γ_j of the j th atom, the exchange interaction $g_{j,k}$ between the j th and k th atoms, and the collective decay rate $\Gamma_{\text{coll},j,k}$ (not studied in this experiment) for the j th and k th atoms are given by

$$\Gamma_j = \sum_{n=1}^{M_j} \sum_{m=1}^{M_j} \sqrt{\gamma_{j_n} \gamma_{j_m}} \cos \phi_{j_n, j_m}, \quad (11)$$

$$g_{j,k} = \sum_{n=1}^{M_j} \sum_{m=1}^{M_k} \frac{\sqrt{\gamma_{j_n} \gamma_{k_m}}}{2} \sin \phi_{j_n, k_m}, \quad (12)$$

$$\Gamma_{\text{coll},j,k} = \sum_{n=1}^{M_j} \sum_{m=1}^{M_k} \sqrt{\gamma_{j_n} \gamma_{k_m}} \cos \phi_{j_n, k_m}. \quad (13)$$

Using this result, we may verify the equations used for the fits. For the first device shown in Fig. 1, we have $N = 2$, $M_1 = M_2 = 2$, $\gamma_{1_1} = \gamma_{1_2} = \gamma_{2_1} = \gamma_{2_2} = \gamma$, and $\phi_{1_1, 2_1} = \phi_{2_1, 1_2} = \phi_{1_2, 2_2} = \phi$. Inserting these into equations (8)–(10), and adding the contribution from decay into modes other than the waveguide γ_{nr} , we recover equations (4) and (5):

$$\Gamma_1 = 2\gamma[1 + \cos(2\phi)] + \gamma_{\text{nr}}, \quad (14)$$

$$g = \frac{\gamma}{2}[3\sin(\phi) + \sin(3\phi)]. \quad (15)$$

Similarly, for the device presented in Fig. 4 we have $N = 2$, $M_1 = M_2 = 3$, $\gamma_{1_1} = \gamma_{1_3} = \gamma_{2_1} = \gamma_{2_3} = \gamma_1$, $\gamma_{1_2} = \gamma_{2_2} = \gamma_2$, $\phi_{1_1, 2_1} = \phi_{1_3, 2_3} = \phi_1$, $\phi_{1_2, 2_2} = \phi_3$ and $\phi_{2_1, 1_2} = \phi_{2_3, 1_3} = \phi_2$. Using these values, we obtain

$$\Gamma_1 = \gamma_2 + 2\gamma_1[1 + \cos(\phi_1 + 2\phi_2 + \phi_3)] + 2\sqrt{\gamma_1\gamma_2}[\cos(\phi_1 + \phi_2) + \cos(\phi_2 + \phi_3)] + \gamma_{\text{nr}}, \quad (16)$$

$$g = \sqrt{\gamma_1\gamma_2}[\sin(\phi_2) + \sin(\phi_1 + \phi_2 + \phi_3)] + \frac{\gamma_1}{2}[2\sin(\phi_1) + \sin(2\phi_2 + \phi_3) + \sin(2\phi_1 + 2\phi_2 + \phi_3)] + \frac{\gamma_2}{2}\sin(\phi_3). \quad (17)$$

and recover equations (6) and (7).

Data availability

The data that support the findings of this study are available from the corresponding author upon reasonable request and with the permission of the US Government sponsors who funded the work.

Code availability

The code used for the analyses is available from the corresponding author upon reasonable request and with the permission of the US Government sponsors who funded the work.

Acknowledgements We thank Y. Sung and A. Greene for valuable discussions. This research was funded in part by the US Department of Energy, Office of Science, Basic Energy Sciences, Materials Sciences and Engineering Division under contract no. DE-AC02-05-CH11231 within the High-Coherence Multilayer Superconducting Structures for Large Scale Qubit Integration and Photonic Transduction programme (QISLBNL); and by the Department of Defense via MIT Lincoln Laboratory under US Air Force contract no. FA8721-05-C-0002. B.K. acknowledges support from the National Defense Science and Engineering Graduate Fellowship programme. M.K. acknowledges support from the Carlsberg Foundation during a portion of this work. A.F.K. acknowledges support from the Swedish Research Council (grant no. 2019-03696), and from the Knut and Alice Wallenberg Foundation through the Wallenberg Centre for Quantum Technology (WACQT). F.N. acknowledges support from the Army Research Office (grant no. W911NF-18-1-0358), the Japan Science and Technology Agency (via the Q-LEAP programme, and CREST grant no. JPMJCR1676), the JSPS KAKENHI (grant no. JP20H00134), the Foundational Questions Institute, and the NTT PHI Laboratory. The views and conclusions contained herein are those of the authors and should not be interpreted as necessarily representing the official policies or endorsements of the US Government.

Author contributions B.K., D.L.C., A.F.K., F.N., S.G. and W.D.O. conceived and designed the experiment. B.K. and D.L.C. designed the devices. B.K. and M.J.R. conducted the measurements, and B.K., M.J.R., A.F.K., J.B. and M.K. analysed the data. D.K.K., A.M., B.M.N. and J.L.Y. performed sample fabrication. B.K. and M.J.R. wrote the manuscript. P.K., A.V. and R.W. assisted with the experimental setup. T.P.O., S.G. and W.D.O. supervised the project. All authors discussed the results and commented on the manuscript.

Competing interests The authors declare no competing interests.

Additional information

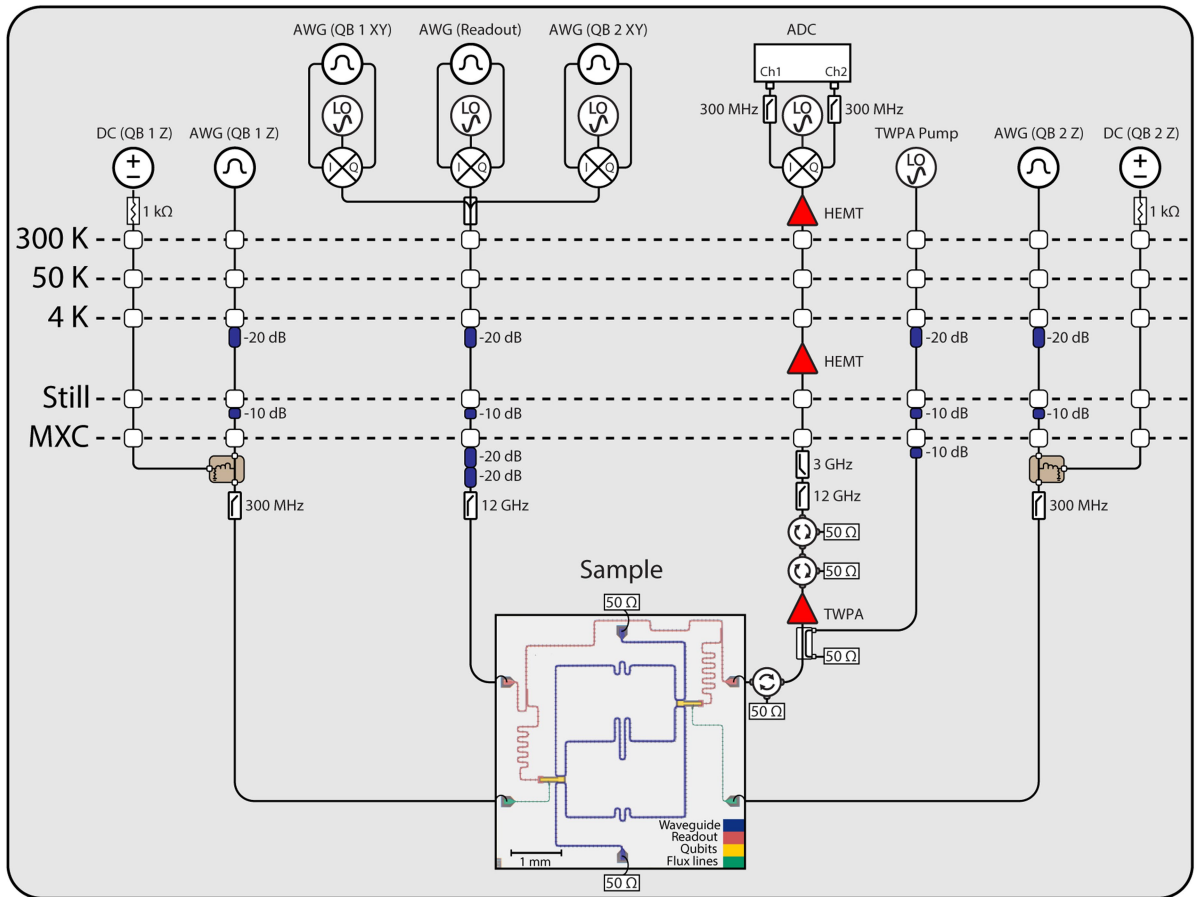
Correspondence and requests for materials should be addressed to B.K. or W.D.O.

Peer review information *Nature* thanks Michael Hartmann, Wolfgang Pfaff and the other, anonymous, reviewer(s) for their contribution to the peer review of this work.

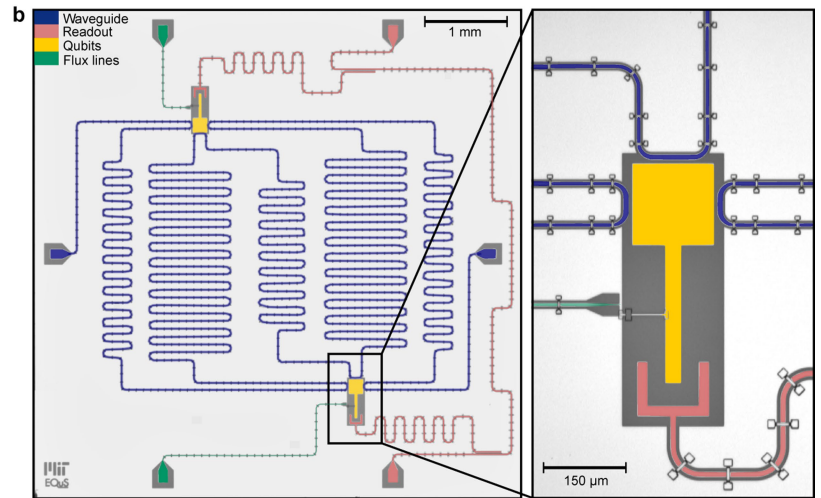
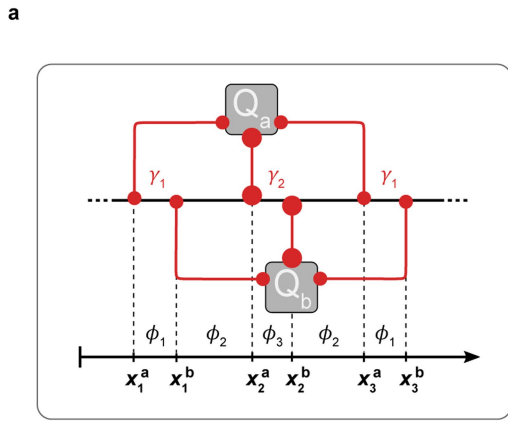
Reprints and permissions information is available at <http://www.nature.com/reprints>.

Article

-  RF Source
-  AWG
-  IQ Mixer
-  DC Source
-  Circulator
-  Amplifier
-  DC + RF Combiner
-  High-Pass Filter
-  Low-Pass Filter
-  Directional Coupler
-  Attenuator
-  Resistor
-  Thermalization



Extended Data Fig. 1 | Experimental setup. A schematic diagram of the experimental setup used to obtain the data presented in the main text.



Extended Data Fig. 2 | Device C. **a**, A schematic diagram of a giant-atom device with two qubits coupled to the waveguide at three points. The ratios ϕ_1/ϕ_2 , ϕ_1/ϕ_3 and ϕ_2/ϕ_3 are fixed in hardware. **b**, A false-colour optical micrograph image of the device in the configuration shown in **a**. Each qubit (yellow) has a

readout resonator (red) and flux line (green) for independent readout and flux control. The central waveguide (blue) is terminated to $50\ \Omega$. Airbridges are placed every $80\ \mu\text{m}$ along the waveguide to tie the ground planes together and prevent slotline modes.

Extended Data Table 1 | Device parameters

Parameter	Device A		Device B		Device C	
	Q _a	Q _b	Q _a	Q _b	Q _a	Q _b
Max Qubit Frequency f_{\max}	4.856 GHz	4.801 GHz	5.403 GHz	5.451 GHz	5.319 GHz	5.371 GHz
Min Qubit Frequency f_{\min}	4.126 GHz	4.109 GHz	4.58 GHz	4.621 GHz	4.101 GHz	4.162 GHz
Junction Asymmetry d	0.903	0.856	0.848	0.852	0.771	0.775
Qubit Anharmonicity $a/2\pi$	-219 MHz	-218 MHz	-213 MHz	-213 MHz	-174 MHz	-175 MHz
T_1 at DF Frequency	31.5 μ s	26.1 μ s	23.5 μ s	29.7 μ s	19.5 μ s	21.2 μ s
T_2^* at DF Frequency	4.2 μ s	3.6 μ s	7.9 μ s	10.8 μ s	5.4 μ s	3.9 μ s
Readout Resonator Frequency f_r	6.982 GHz	7.161 GHz	6.984 GHz	7.166 GHz	7.094 GHz	7.287 GHz
Dispersive Shift χ	0.577 MHz	0.463 MHz	1.09 MHz	0.911 MHz	0.518 MHz	0.441 MHz
Readout Resonator Linewidth $\kappa/2\pi$	0.95 MHz	0.693 MHz	0.971 MHz	0.698 MHz	0.575 MHz	0.491 MHz

Summary of the qubit and readout parameters for the devices used in the data presented in Figs. 2–4. Devices A and B are of the same design and were used for the data in Figs. 2, 3. Device C was used for the data in Fig. 4. The relaxation times T_1 and Ramsey coherence times T_2^* are quoted at the waveguide decoherence-free (DF) frequency. All other frequency-dependent parameters are quoted at the maximum qubit frequency.